An analytical solution for wind deficit decay behind a wind energy converter using momentum conservation validated by UAS data

Moritz Mauz[1], Bram van Kesteren[1], Andreas Platis[1], Stefan Emeis[2], and Jens Bange[1]

[1]Centre for Applied Geoscience, University of Tübingen, 72074 Tübingen, Germany
[2]Institute for Meteorology and Climate Research, Karlsruhe Institute of Technology, 82467 Garmisch-Partenkirchen, Germany

Correspondence: Moritz Mauz (moritz.mauz@uni-tuebingen.de)

Abstract. The wind deficit behind a wind energy converter (WEC) results from a complex interaction of forces. Kinetic energy is removed from the atmosphere, but coherent turbulent structures prevent a swift compensation of momentum within the wake behind the WEC. A detailed description of the wake is beneficial in meso-scale weather forecast (e.g. WRF models) and numerical simulations of wind wake deficits. Especially in the near to intermediate wake ($0.5 - 5$ rotor diameters D), the dominating processes characterising the wake formation change along the wake. The conservation equation of momentum is used as a starting point to map the most important processes assuming the WEC operates at maximum efficiency in a neutral stratified boundary layer. The wake is divided into three different regions to accommodate the changing impact of atmospheric turbulence and the shear created by the WEC onto the wake. A differential equation that depicts the variable momentum transport into the wind deficit along the wake is derived and solved analytically. Additionally, a numerical solution (Euler method) of the simplified momentum conservation equation is shown to provide a quality control and error estimate to the analytical model. The analytical solution is compared to conventional WEC wake models and in-situ wake measurements behind an Enercon E-112 converter, located in the Jade Wind Park near the North Sea coast in Germany, captured by the MASC-3 UAS (unmanned aircraft system) of the University of Tübingen. The obtained UAS data cover the distance from $0.5 - 5$ D at hub height behind the nacelle. The analytical and numerical model are found to be in good agreement with the data of the three measurement flights behind the WEC.

1 Introduction

Wind energy converters (WECs) remove kinetic energy from the mean flow in the atmosphere which results in a wind deficit in the wake behind each converter. The interaction of these individual wakes with the atmosphere and even with neighbouring converters needs to be understood, for example in order to increase wind park efficiency (Stevens, 2016). With increasing sizes of WECs and wind farms, the wind deficit created by the wind parks and individual converters affects the environment increasingly. The WIPAFF (Wind PArk Far Field) project determined the length of single wind park wakes and found their dimensions

large enough to influence local wind conditions (Platis et al., 2018; Bärfuss et al., 2019). Platis et al. (2018) observed different wind park wake lengths with varying thermal atmospheric stability. Therefore, a mutual influence between local weather and neighbouring wind farms is likely. WRF (weather research and forecasting model) simulations by Siedersleben et al. (2018) display the wind deficit using wind farm parametrisation (WFP). Emeis (2010) introduced a wind deficit model for wind farms,

5 concluding that the wind deficit decreases because of momentum inflow from higher altitudes. Therefore the atmosphere itself, e.g. its thermal stratification and turbulent momentum flux have an influence onto the WEC wake development (Johnson et al., 2014). The Lagrangian approach by Emeis (2017) leads to a time dependent solution for an exponential decrease of the wind deficit. While clustered WECs and their wind deficit have an influence on the meso-scale weather, individual WECs influence the atmospheric flow and turbulent transports on a smaller scale in their respective wake area. A key parameter is to resolve

10 the wind deficit as a main driver of shear stress in the wake. In numerical simulations wind deficit models based on the thrust coefficient of the WEC are common practice. For example Magnusson and Smedman (1999) describe the wind deficit as a time dependent exponential function. Bastankhah and Porté-Agel (2014) also propose a far wake wind deficit model using the thrust coefficient of the energy converter. Their model is an extension of the analytical wake model by Frandsen et al. (2006). They also use an additional wake widening parameter or growth rate k, originally introduced by Jensen (1983), to obtain a

15 more precise prediction in the far wake. While the model by Bastankhah and Porté-Agel (2014) provides a spatial distribution for the wind deficit, together with all aforementioned single WEC models, it lacks atmospheric boundary conditions (turbulence, thermal stratification etc.) that have an influence on the wake development (Wu and Faeth, 1994; Johnson et al., 2014). Bastankhah and Porté-Agel (2017) refined their analytical model utilising wind-tunnel data, however, atmospheric conditions are hard to simulate in wind-tunnel experiments. Usually, wind-tunnel results suffer from scaling errors when applied to the

20 real world (Wang et al., 2020). Yet, for the simulated conditions (thermally neutral stratification and along the dimensions of the wind-tunnel) the model from Bastankhah and Porté-Agel (2017) works fine for distances $x/D > 3$. This empirical model is fast and computationally inexpensive but it remains a model that is decoupled from any atmospheric input.

In this work an approach is proposed that combines findings from Medici and Alfredsson (2006) and Frandsen (2007) that link the decay of the tip-vortex helix (at the boundary of the near and intermediate wake, approximately at a distance of

25 $2 - 3$ D) with an increase of wind deficit decay. Up to this region the tip-vortex helix acts as a shield against atmospheric turbulence in-flux (Frandsen, 2007; Lignarolo et al., 2014). The proposed analytical model will connect the near wake with the mid and far wake wind deficit. A non-linear wind deficit decay rate α will be introduced and a first description is shown. In the following, the MaST (Mauz Single Turbine) wake model, a steady-state spatial analytical solution for a wind deficit is presented, based on the momentum conservation equation and based on some assumptions. A numerical calculation using

30 the implicit and explicit Euler method are made to validate the simplification made to solve the resulting differential equation. This model aims for a more precise description of WEC wakes, especially from the atmosphere's point of view. While many analytical wake models exist, none of them implements atmospheric conditions and regards the wind deficit only as a result of the momentum sink that the WEC represents. Thus, those models are an analytical representation of a mechanical process, but commonly lack realistic turbulence-related phenomena originating from the surrounding atmosphere that influence the wake

35 development. Consequently, the proposed model is an addition to existing models that describe WEC deficits directly behind

the WEC using thrust coefficient based calculations. The model does not use WEC parameters as e.g. the thrust coefficient. Instead it is assuming that the WEC is running in optimal condition and that Betz (1920) theory is applicable. The only WEC parameter going into the model is the rotor diameter D of the WEC.

In the present study in-situ UAS (unmanned aircraft system) based wake measurements are used to display the wind deficit

5   behind an Enercon E-112 converter in the near to mid wake (0.5 to 5 rotor diameters D) and to measure the initial conditions in the surrounding atmospheric flow. The MASC UAS platform was successfully used in previous measurement campaigns (Mauz et al., 2019; Rautenberg et al., 2019; Braam et al., 2016; Wildmann et al., 2015, 2014a). The obtained data is compared to the WEC wake models from Frandsen et al. (2006) or Bastankhah and Porté-Agel (2014, 2017).

In the context of this study, in-situ measurements have the advantage that the measured wind is already a superimposition

10   of turbulence created by the WEC and the free-stream turbulence. Consequently, a model derived from UAS in-situ data needs to accommodate turbulence and shear terms in some way. Disadvantages of real-world experiments are, of course, additional boundary conditions that are hard to quantify, e.g. vegetation, additional WECs or obstacles of any kind (dyke, buildings) creating random, unrelated (to the investigated phenomenon) turbulence that adds uncertainties to the wake measurement.

2   Theory and methods

15   ### 2.1   Conventional engineering wake models

As a comparison two established analytical models are used with airborne measured data. The first one is the Frandsen et al. (2006) wake model where residual wind velocity u_r normalised with the free stream velocity u_0 at hub height and at distance x in the wake of a WEC with rotor diameter D is given by:

$$\frac{u_r}{u_0} = \frac{1}{2}\left(1 + \sqrt{1 - \frac{2C_T}{\beta + Kx/D}}\right) \tag{1}$$

20   K is in the order of $10\,k$, with k the wake growth rate:

$$k \approx \frac{0.5}{\ln(h/z_0)}, \tag{2}$$

and h the hub height of the WEC and z_0 the roughness height. The model uses a parameter β that relates to the thrust coefficient C_T of the WEC.

$$\beta = \frac{1 + \sqrt{1 - C_T}}{2\sqrt{1 - C_T}} \tag{3}$$

25   The second analytical model is a modification of the Frandsen model by Bastankhah and Porté-Agel (2014) derived from wind tunnel measurements. The normalised residual wind speed in their model is described by:

$$\frac{u_r}{u_0} = \sqrt{1 - \frac{C_T}{8(\sigma/D)^2}}, \tag{4}$$

where σ is the lateral wake width. In this model a linear wake growth k is assumed.

$$\frac{\sigma}{D} = k\frac{x}{D} + \epsilon \tag{5}$$

The initial wake width ϵ is equal to $0.2\sqrt{\beta}$ (Bastankhah and Porté-Agel, 2014).

2.2 The MaST model: a likely analytical solution of the conservation of momentum equation

5   The starting point for the presented analytical wind deficit model is the equation for conservation of momentum in the mean flow using Einstein summation notation (Stull, 1988). After Reynolds averaging and the Boussinesq approximation have been applied, the conservation of momentum can be written as:

$$\underbrace{\frac{\partial \overline{u_i}}{\partial t}}_{\text{I}} + \underbrace{\overline{u_j}\frac{\partial \overline{u_i}}{\partial x_j}}_{\text{II}} + \underbrace{\delta_{i3}g}_{\text{III}} - \underbrace{f_c\epsilon_{ij3}\overline{u_j}}_{\text{IV}} + \underbrace{\frac{1}{\overline{\rho}}\frac{\partial \overline{p}}{\partial x_i}}_{\text{V}} - \underbrace{\frac{\nu\partial^2\overline{u_i}}{\partial x_j^2}}_{\text{VI}} + \underbrace{\frac{\partial \overline{u_i'u_j'}}{\partial x_j}}_{\text{VII}} = 0 \tag{6}$$

Here, $i, j = 1, 2, 3$ for all three directions in space, g is the gravitational acceleration, p the static pressure, f_c the Coriolis
10   parameter, ν the kinematic viscosity and ρ the density of air.

     Term I   represents storage of mean momentum.
     Term II   describes advection of mean momentum by the mean wind.
     Term III   allows gravity to act in the vertical direction only.
     Term IV   describes the influence of the Coriolis force.
     Term V   describes the mean pressure-gradient force.
     Term VI   represents the influence of viscous stress on the mean motions assuming incompressibility.
     Term VII   represents the influence of Reynolds' stress on the mean motions.

     A one dimensional, horizontal steady-state wind field ($i = 1$) with no buoyancy is assumed (no local change in wind direction and wind speed at each location and time). No meso-scalic changes in the static pressure gradient occur in the model. Thus,
15   term I, III and term V can be cancelled from the equation. In this study the wake is observed up to $5\,\mathrm{D} \approx 600\,\mathrm{m}$ only, thus the Coriolis force (term IV) can be neglected. Term VI represents the viscous stress and observations in the atmosphere indicate that the molecular diffusion is several order of magnitudes smaller compared to the other terms and can be neglected (Stull, 1988). Equation 6 can now be simplified. The mean reduced horizontal wind speed $\overline{u}$ in the wake at hub height in x-direction along the wake centre line for an incompressible flow, with the remaining terms II and VII, can be approximated as:

$$\overline{u}\frac{\partial \overline{u}}{\partial x} + \overline{v}\frac{\partial \overline{u}}{\partial y} + \overline{w}\frac{\partial \overline{u}}{\partial z} = -\frac{\partial \overline{u'u'}}{\partial x} - \frac{\partial \overline{u'v'}}{\partial y} - \frac{\partial \overline{u'w'}}{\partial z} \tag{7}$$

     Applying the product rule to each term on the left hand side of Eq. 7 yields:

$$\overline{u}\frac{\partial \overline{u}}{\partial x} = \frac{\partial \overline{u}^2}{\partial x} - \overline{u}\frac{\partial \overline{u}}{\partial x}; \tag{8}$$

$$\overline{v}\frac{\partial \overline{u}}{\partial y} = \frac{\partial(\overline{u}\,\overline{v})}{\partial y} - \overline{u}\frac{\partial \overline{v}}{\partial y}; \tag{9}$$

$$\overline{w}\frac{\partial \overline{u}}{\partial z} = \frac{\partial(\overline{u}\,\overline{w})}{\partial z} - \overline{u}\frac{\partial \overline{w}}{\partial z}; \tag{10}$$

The left side of Eq. 7 can now be rewritten as:

$$\frac{\overline{u}^2}{\partial x} - \overline{u}\frac{\partial \overline{u}}{\partial x} + \frac{\partial(\overline{u}\,\overline{v})}{\partial y} - \overline{u}\frac{\partial \overline{v}}{\partial y} + \frac{\partial(\overline{u}\,\overline{w})}{\partial z} - \overline{u}\frac{\partial \overline{w}}{\partial z}$$

$$= \frac{\overline{u}^2}{\partial x} + \frac{\partial(\overline{u}\,\overline{v})}{\partial y} + \frac{\partial(\overline{u}\,\overline{w})}{\partial z} - \overline{u}\underbrace{\left[\frac{\partial \overline{u}}{\partial x} + \frac{\partial \overline{v}}{\partial y} + \frac{\partial \overline{w}}{\partial z}\right]}_{=0} \tag{11}$$

Since a steady-state incompressible flow is considered, the part in brackets in Eq. 11 is zero (divergence-free flow). The left

5   side of Eq. 7 can now be written using Eq. 11.

Now, we focus only on the wake. Therefore we denote the residual wind speed in the wake along the centre line $\overline{u} = u_r$. Finally Eq. 12 is the momentum conservation equation along x in differential form for an incompressible steady-state flow (Lecheler, 2011).

$$\underbrace{\frac{\partial(u_r \cdot u_r)}{\partial x}}_{A} + \underbrace{\frac{\partial(\overline{v} \cdot u_r)}{\partial y}}_{B} + \underbrace{\frac{\partial(\overline{w} \cdot u_r)}{\partial z}}_{C} = -\underbrace{\frac{\partial(\overline{u'u'})}{\partial x}}_{D} - \underbrace{\frac{\partial(\overline{u'v'})}{\partial y}}_{E} - \underbrace{\frac{\partial(\overline{u'w'})}{\partial z}}_{F} \tag{12}$$

10   The downstream velocity in the wake increases with distance ($\partial u/\partial x > 0$). Considering the general continuity equation we have:

$$\frac{\partial v}{\partial y} + \frac{\partial w}{\partial z} = -\frac{\partial u}{\partial x} \tag{13}$$

If furthermore a circular symmetric wake is assumed and comparable flow conditions below, left and right to the wake exist due to the initial flow conditions surrounding the wake with $du_0/dz \approx 0$ (s.a Fig. 1), then at the wake centre line the following

15   is true:

$$\frac{\partial v}{\partial y} = \frac{\partial w}{\partial z} \rightarrow 2\frac{\partial v}{\partial y} = -\frac{\partial u_r}{\partial x} \tag{14}$$

The left hand side (term A, B and C) of Eq. 12 at the centre line can now be simplified using Eq. 14:

$$\frac{\partial(u_r \cdot u_r)}{\partial x} + \underbrace{u_r\frac{\partial \overline{v}}{\partial y} + u_r\frac{\partial \overline{w}}{\partial z}}_{u_r\left(2\frac{\partial v}{\partial y}\right) = -u_r\frac{\partial u_r}{\partial x}} + \underbrace{\overline{v}\frac{\partial u_r}{\partial y}}_{=0} + \underbrace{\overline{w}\frac{\partial u_r}{\partial z}}_{=0} = 2u_r\frac{\partial u_r}{\partial x} - u_r\frac{\partial u_r}{\partial x} = u_r\frac{\partial u_r}{\partial x} = \frac{1}{2}\frac{\partial u_r^2}{\partial x} \tag{15}$$

Note that due to the circular symmetry and the convergence towards the wake centre line the lateral velocity components must

20   be zero there ($v|_{y=0} = w|_{y=0} = 0$). If this were not the case the whole wake would be moved away from the rotor axis of the WEC and the centre line were no longer identical to the rotational axis of the WEC.

Coming now to the right hand side of Eq. 12 or the divergence of the turbulent fluxes of the longitudinal velocity perturbation u'. Recalling the rotational symmetry of the wake and the initial conditions with $du_0/dz \approx 0$ the lateral flux perturbations (term E in Eq. 12) are identical to the vertical perturbations (term F). Concerning term D it is common, to neglect this longitudinal

change (i.e. in x-direction) of the longitudinal turbulent flux of longitudinal momentum in comparison to $\partial u_r^2/\partial x$. Equation 12 can now be rewritten:

$$\frac{\partial u_r^2}{\partial x} + 4\frac{\partial(\overline{u'w'})}{\partial z} = 0 \tag{16}$$

Equation 6 is now reduced to a much simpler differential equation in one dimension by cancelling insignificant parts, consider-
ing the order of magnitude of each term. The resulting Eq. 16 states that a change in the wind speed in x direction corresponds to a change of vertical momentum (in-)flux. This equation is the Eulerian analogy to Eq. 17 in Emeis (2010) using a Lagrangian approach.

To further simplify the approach, an empirical relation (Gradient method) is applied, assuming a first order distribution of the Reynolds shear stress along z. Therefore, the Reynolds shear stress can be expressed using a momentum transfer coefficient
K_m and can be brought to a finite difference form at the wake centre line at height h:

$$\frac{\Delta\overline{u'w'}}{\Delta z} = \frac{\overline{u'w'}(h+\Delta z/2) - \overline{u'w'}(h-\Delta z/2)}{\Delta z} \tag{17}$$

In order to obtain the flux-divergence at height h for all x, assuming a symmetric wake flow above and below the centre line, the resulting form is:

$$\frac{\Delta\overline{u'w'}}{\Delta z} = -K_m\frac{(u_0-u_r)/\Delta z - (u_r-u_0)/\Delta z}{\Delta z} = -2K_m\frac{u_0-u_r}{\Delta z^2} \tag{18}$$

With these bulk simplifications and going from ∂ to d, Eq. 16 is now of the form:

$$\frac{du_r^2}{dx} = -8K_m\frac{u_0-u_r}{\Delta z^2} = \underbrace{\frac{-CK_m}{\Delta z^2}}_{\alpha}(u_0-u_r) = \alpha(u_0-u_r), \text{ with } C = 8 \tag{19}$$

With $\Delta u = u_0 - u_r$ the difference between the undisturbed wind speed u_0 and the reduced wind speed u_r in the wake. The newly introduced parameter α is the wind deficit decay rate. For now, it will be treated as a constant. An additional solution with a changing rate α along x, will also be introduced and discussed. Due to the rotational symmetry Δz will be renamed to the
turbulence thickness d that describes the thickness of a volume that consists solely of turbulence created by the WEC. Through this volume of thickness d the wind speed is reduced to u_r and momentum is transported into the wake. Above $z = h + d$ an undisturbed flow velocity u_0 is assumed which varies only little with height (see Fig. 1). C is a parameter derived from the model geometry, describing the momentum influx over the circular symmetric surface. This means for $C = 8$ momentum influx from all sides is equally pronounced. In reality this is not the case and will be discussed later. K_m is the momentum
transfer coefficient (s.a. Sec. 2.3).

To get an analytical solution, Eq. 19 needs now to be solved:

$$\frac{du_r^2}{dx} = \alpha u_0 - \alpha u_r \Longleftrightarrow 2u_r \frac{du_r}{dx} = \alpha u_0 - \alpha u_r$$

Rearranging and moving dx to the other side

$$\Longleftrightarrow du_r = \left(\frac{\alpha u_0}{2u_r} - \frac{\alpha}{2} \right) dx \tag{20.1}$$

5   integrating over du_r on the left and over dx on the right yields:

$$\Longleftrightarrow u_r = \left(\frac{\alpha u_0}{2u_r} - \frac{\alpha}{2} \right) x + c$$

Equation 19 is the difference form of a non-homogeneous non-linear differential equation (DE) of first order. The solutions u_r^{hom} of the corresponding homogeneous DE are of the form:

$$u_r^{\mathrm{hom}} = \pm \sqrt{\alpha \, u_0 \, x} \tag{20.2}$$

which actually is vividly realistic: the reduced wind speed u_r increases by the square-root of the horizontal distance x - quite similar to the vertical development of turbulent boundary layer or an internal boundary layer in heterogeneous terrain (Garratt, 1987, 1994; Hanna, 1987). However, a particular solution of the non-homogeneous DE 19 could not be found. In order to find an approximated solution, u_r is treated as a constant on the right-hand side of Eq. 20.1 and the simplified DE is solved in the following. The obtained result agrees sufficiently well with the numerical solution introduced later (s. App. A).

Additionally, a short assessment of the order of magnitude assures that the introduced error by treating u_r as a constant for the integration step, is given. It is assumed that the change of the velocity gradient along x is small (with the velocity gradient in the order of $\frac{u_0 - u_r(0)}{1000 \text{ m}} \approx \frac{7}{1000} \text{ s}^{-1}$). This complies with Taylor's hypothesis of frozen turbulence, similarly implemented in the model by Emeis (2010, 2017). This will introduce a small error, as afore mentioned, a comparison with a numerical solution of Eq. 20.1 will be shown in the results. Using the described simplification, the analytical solution is much more convenient to solve, and the introduced error is small.

Rearranging again and multiplying with u_r

$$\Longleftrightarrow u_r^2 + \frac{\alpha u_r x}{2} - c u_r - \frac{\alpha u_0 x}{2} = 0$$

rewrite as a quadratic equation

$$\Longleftrightarrow u_r^2 + u_r \left(\frac{\alpha x}{2} - c \right) - \frac{\alpha u_0 x}{2} = 0 \tag{20.3}$$

10 This quadratic equation has two solutions:

$$u_{r_{1,2}}(x) = \frac{1}{2} \left(\left(c - \frac{\alpha x}{2} \right) \pm \sqrt{ \left(\frac{\alpha x}{2} - c \right)^2 + 2u_0 \alpha x } \right) \tag{21}$$

While only the positive solution is physically relevant, resulting in positive wind speeds, c can now be determined using initial boundary conditions, i.e. for $x = 0$. The initial conditions can be measured or a theoretical value can be taken, e.g. $u_r(0) \approx 0.3\, u_0$ using Betz law (Betz, 2013), resulting in $c = 0.3\, u_0$.

When examining a wind deficit created by a single converter, a closer look on the deficit formation is necessary. The different

5   wake regions can be divided in three areas that, in numerical modelling, need different approaches (s.a. Fig. 1): the near, intermediate and the far wake (Brand et al., 2011). Directly behind the nacelle, in the near wake, a low pressure region expands up to $2 - 3$ D until ambient pressure levels are reached again. After this point, up to 10 D in the intermediate wake, radial flow shear starts to drain turbulence and the wind deficit is beginning to be reduced (Medici and Alfredsson, 2006; Frandsen, 2007). Note that the radial shear stress is represented by the combined vertical and horizontal shear in this approach (Eq. 16). In the

10   intermediate wake, the wind deficit starts to decay and turbulence and momentum flux gradients begin to decrease. In the far wake (10 to 20 D), the wind deficit dissipates. The above mentioned wake regions are not rigid and depend on the mean wind speed, thermal stratification, surface roughness etc.

In the presented approach, the wind deficit of a single turbine is described by the vertical momentum flux. And since the near wake and the intermediate wake are of interest, a closer look onto the turbulence distribution inside these parts of a wake, is

15   necessary. Frandsen (2007) describes how the wind deficit is reduced by ambient turbulence acting from the wake boundaries (s.a. green arrows in Fig. 1). The wake can now be divided in turbulence created by the wind deficit (s.a. purple volume in Fig. 1) and a mix of atmospheric and wake turbulence that has 'forgotten its origin' in the outer regions of the wake. Hence, in a wake, the area inhabiting turbulence created by the wind deficit, is a rotational symmetric volume that slowly becomes smaller, as the distance to the nacelle increases (approximately up to 10 D).

20   The model has to consider that the deficit decay depends on the distance x. Therefore, the wind deficit decay rate α (see Eq. 19) is modified to increase with increasing distance from the nacelle in the wake. In practice, this is implemented by an approximation of the thickness of the core wake, that is still untouched by the free-stream turbulence (s.a. Eq. 22) and is shown by the purple volume in Fig 1. Equation 22 is a hyperbolic function. In a first approach this asymptotic function has been chosen to represent the remaining WEC turbulence along x. This is an educated guess, since the remaining turbulence (in this model

25   approach) needs to decay from R to 0 in some manner. Then, for the one-dimensional approach in this study, the thickness of this rotational symmetric volume is identical to a 'turbulence thickness' $d(x)$:

$$d(x) = \frac{2\mathrm{D}^2}{x + 2\mathrm{D}} \tag{22}$$

For this study, with the available data, the distance at which the free-stream turbulence caves into the wake is approximately two rotor diameters (Medici and Alfredsson, 2006; Frandsen, 2007). Conclusively, a new function $d(x)$ is needed. Considering

30   all requirements to the new relation, Eq. 25 is formulated. This equation is not continuously differentiable, hence the kink in its analytical solution (Fig. 2). In the real world this boundary would be fluent (cf. the numerical solution in Fig. 7). The 'dynamic alpha' analytical solution is computed in a semi-numerical way, this means that $\alpha(x)$ is calculated using Eq. 23 for each distance and then inserted into Eq. 21. A sole analytical solution is possible inserting Eq. 25 into Eq. 20.1. However, for this proof of concept with the Euler method as validation (s.a. App. A), the more convenient and easy to implement method of
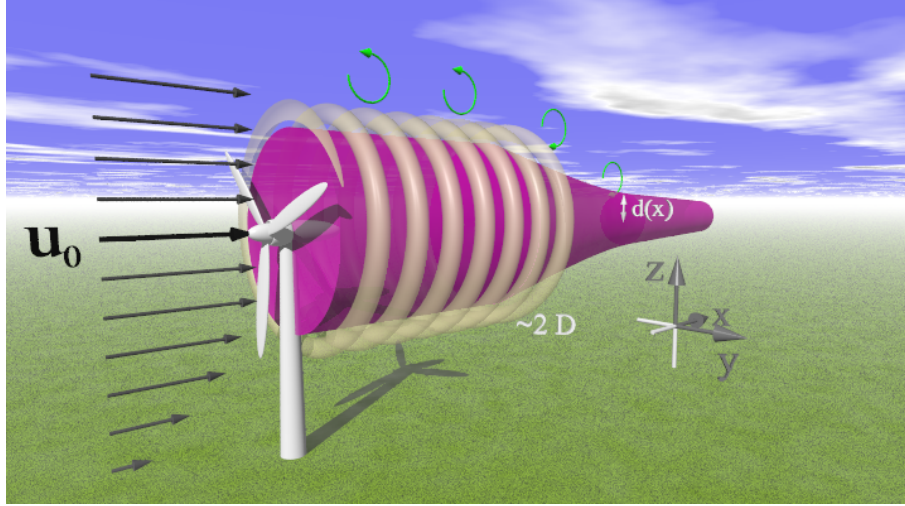
Figure 1. Sketch of a WEC wake, the incoming wind profile with u_0 at hub height, and the wake turbulence development (not true to scale). The coherent helical tip vortex structures (beige) prevents atmospheric turbulence (green arrows) to enter the wake up to about $2\,D$. After this point, the helical tip vortex structure begins to decay and atmospheric turbulence (green arrows) can enter the wake. The area inhabiting turbulence 'knowing its origin' from the WEC thins out with increasing distance to the nacelle (purple volume).

the semi-numerical solution is used.

$$\alpha(x) = \frac{C \cdot K_\mathrm{m}}{d(x)^2} \tag{23}$$

$\alpha = \text{constant}$		$\alpha = \text{dynamic}$	
$d(x) = \dfrac{1}{2}\,D$	(24)	$d(x) = \begin{cases} \dfrac{1}{2}\,D & \text{if } x \leqq 2\mathrm{D} \\[2mm] \dfrac{2\mathrm{D}^2}{x+2\mathrm{D}} & \text{if } x > 2\mathrm{D} \end{cases}$	(25)

2.3 The momentum transfer coefficient K_m

5 For the calculations presented later in this study, K_m needs to be resolved:

$$K_\mathrm{m} = \kappa \cdot u_* \cdot z \tag{26}$$

With u_* the friction velocity at the surface, altitude z and κ the von Kármán constant Eq. 26 is valid in the surface layer (Emeis, 2010; Foken, 2006). For the sake of this derivation and the assumption that the error is small, it is assumed that Eq. 26 can be applied (s.a. Sec. 5). The friction velocity is computed from a vertical profile that was measured in front of the WEC in the

10 inflow. Details are given in Sec. 3.3. In Sec.5 the sensitivity of the model towards u_* is discussed.
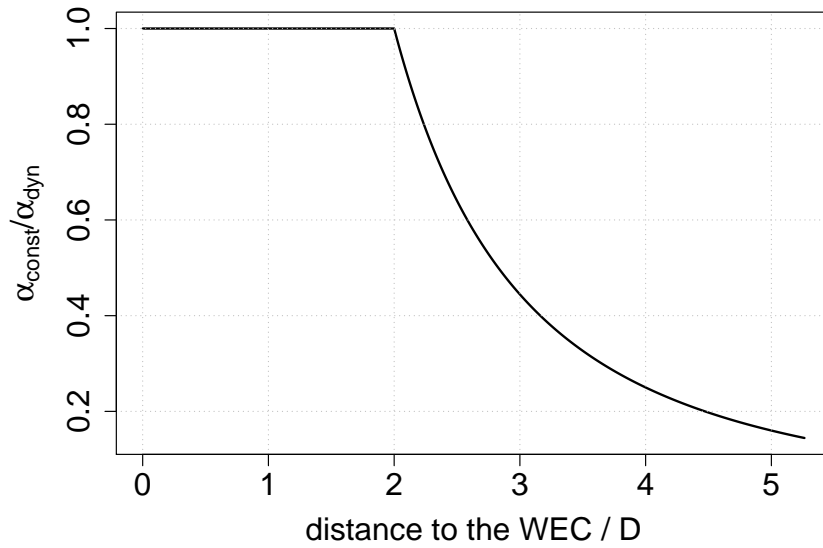
Figure 2. Ratio of the dynamic and constant wind deficit decay rate α. Increasing α_{dyn} values lead to a faster wind deficit decay along the wake. A coherent tip vortex helix up to approximately 2 D, shields the wind deficit from free-stream turbulence caving in. From thereon onwards, wake turbulence and atmospheric turbulence begin to interfere.

3 Data acquisition and data treatment

3.1 Measurement system

All data were captured using the in-house developed MASC (multi-purpose airborne sensor carrier) small UAS of the University of Tübingen. With a wingspan of roughly 4 m it can carry a payload of 2.5 kg and fly autonomously up to 2 hours using the Pixhawk 2.1 autopilot (Pixhawk-Organisation, 2019), propelled by an electrical pusher motor. MASC is equipped with a five-hole probe to resolve turbulent pressure fluctuations, GPS and a platinum fine wire resistance thermometer at the nose of the UAS (s.a. Fig. 3). With its set-up it is possible to calculate the 3-D wind vector at any point in space up to 30 Hz. The vertical path accuracy is about ± 2.5 m, the horizontal path accuracy with the standard GPS positioning around ± 0.75 m in a highly turbulent conditions. A more detailed description of the UAS and its instrumentation can be found in Rautenberg et al. (2019). Previous measurement campaigns, including wind energy research based on MASC-3 measurements can be found in Mauz et al. (2019); Wildmann et al. (2014a, b, 2013).
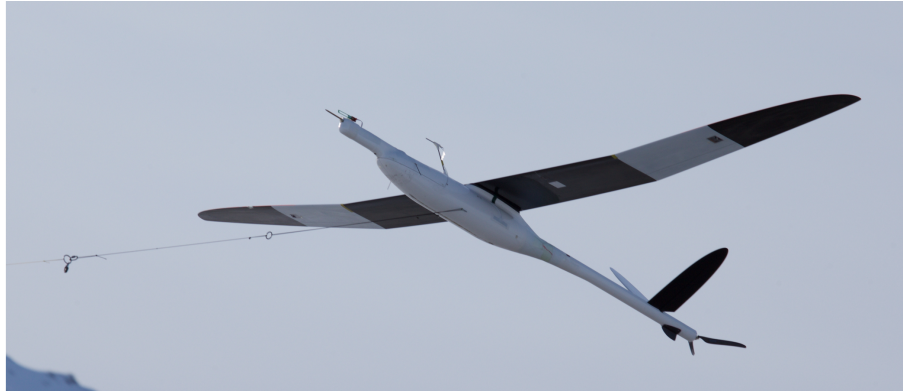
Figure 3. In-house built small UAS of type MASC of the University of Tübingen shortly after lift-off. At the front of the UAS the five hole probe and the fine wire resistor thermometer are visible. The air plane is propelled by an electrical pusher motor.

3.2 Experimental site

The underlying in-situ data were captured behind an Enercon E-112 converter that is part of the Jade wind park north of Wilhelmshaven in Germany. The WEC is located roughly 2 km from the North Sea coast line. In mid November 2019 a measurement campaign took place for the HeliOW (helicopter flights in off-shore wind parks) project funded by the BMWi

5 (Federal Ministry of Economic Affairs and Energy in Germany). The project aims to determine safe helicopter corridors in offshore wind parks, since wind parks are getting larger and single WECs continue to increase in dimensions. The wind measurements form the foundation for a numerical simulation chain that investigates the impact of blade tip vortices and wake turbulence on helicopter flight dynamics (Horvat et al., 2020) from numerical simulated wake data (Cormier et al., 2018), accompanied with piloted simulations using the AVES helicopter flight simulator at the German Aerospace Center (Strbac

10 et al., 2019). At a previous campaign in 2018, measurement strategies were tailored toward measuring blade-tip vortices (Mauz et al., 2019); whereas in the recent campaign the goal was to cover the wind deficit in the near to intermediate wake at hub height. To accomplish this, a meander pattern was flown by the UAS covering the wake from 0.5 D to 5 D (Fig. 4), legal restrictions prevented farther downstream reaching measurements. Altogether, three consecutive flights are available for different flight legs behind the WEC at hub height. A so called leg is the straight and level flight path in a measurement flight

15 pattern. But as it turned out, in flight 1 the legs were too short to cover the whole wake downstream, thus in flight 1 the number of measurement legs is reduced to the ones in the near wake. Due to high wind speeds the UAS needed a larger turning circle as usual and the flight pattern needed adjustment (s.a green tracks in Fig. 4). The E-112 was operating near its rated conditions.

3.3 Atmospheric conditions

20 The measurement flights took place November 15, 2019, at 15:30 LT in the Jade wind park with an easterly wind direction. An average wind velocity of $11.0 \, \mathrm{m\,s^{-1}}$ with a deviation of $\pm 1.5 - 2 \, \mathrm{m\,s^{-1}}$ at hub height behind the WEC was measured
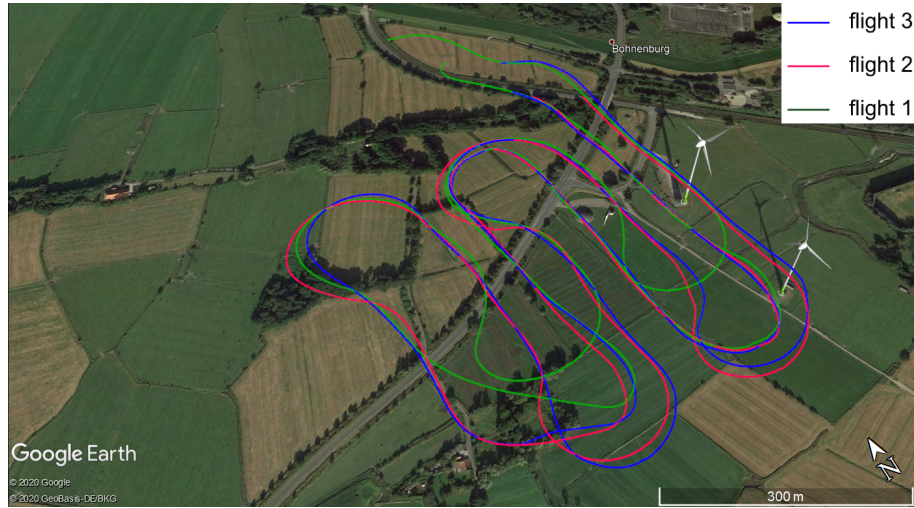
Figure 4. Flight paths of the MASC-3 UAS at hub height in the wake behind the E-112 WEC (northern converter). The measurement legs of flight 1 (green line) were too short, thus the legs were extended for the second and third flight (red and blue line). Therefore, limited data are available for flight 1. The WEC in the south did not interfere with the measurements.

with gusts up to $\approx 13\ \mathrm{m\ s^{-1}}$. The turbulence intensity (TI) at this altitude was about $5 - 8\ \%$. It is computed by calculating $\mathrm{TI} = u'_{\mathrm{hor}}/\overline{u_{\mathrm{hor}}}$ from a vertical profile flown in the inflow of the WEC directly before Flight 1. With u_{hor} being the horizontal wind. The averaging window is derived from the computed integral length scale (e.g. around hub height). Figure 5 shows a vertical profile of the virtual potential temperature in the inflow that suggests near neutral conditions above 20 m a.g.l. The vertical profile of the horizontal wind in front of the WEC is shown by black dots. The black solid line is the moving average of the horizontal wind along 500 data points. While the temperature profile suggests a neutral atmospheric stratification the wind profile of the first 50 m resembles a profile that fits to a stable stratification. However, we assume this anomaly is caused by the vicinity to the dyke that reshapes the wind profile in the lower altitudes.

The friction velocity u_* is calculated from the wind data up to 20 m a.g.l resulting in:

$$u_* = \sqrt{-\overline{u'w'}} = 0.29\ \mathrm{m\ s^{-1}} \tag{27}$$

The measured friction velocity is used for a logarithmic fit of the wind data in front of the WEC using:

$$u(z) = \frac{u_*}{\kappa} \ln\left(\frac{z}{z_0}\right), \text{ with } \kappa = 0.4,\ u_* = 0.29\ \mathrm{m\ s^{-1}},\ z_0 = 0.0001\ \mathrm{m} \text{ and } z \text{ the altitude over ground.} \tag{28}$$

The resulting fit suggests a wind profile that is dominated by marine conditions ($z_0 = 0.0001$ m), which is realistic due to the vicinity to the North Sea and the easterly wind direction.

WIND
ENERGY
SCIENCE
DISCUSSIONS
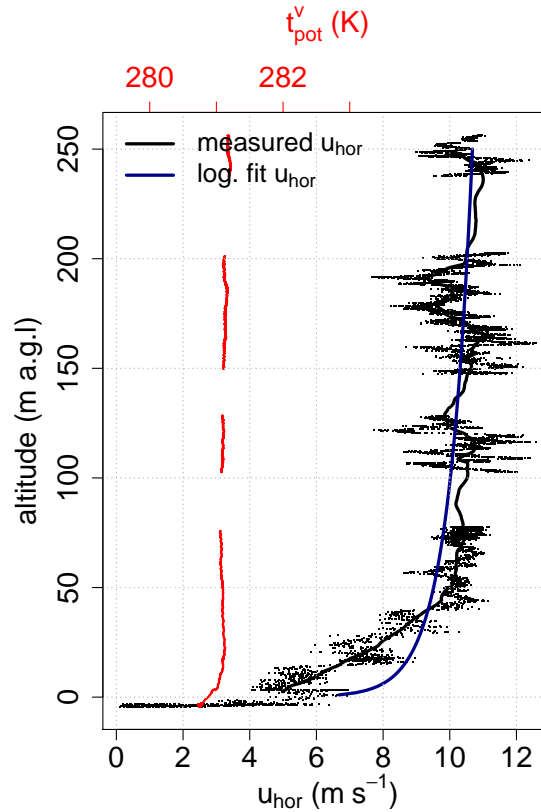
Figure 5. Vertical profiles of the potential virtual temperature (red line) and of the horizontal wind u_{hor} about 2 D in front of the WEC (black dots), the black solid line is a moving average of over 300 data points or 3 seconds. The grey line is a logarithmic fit of the wind measurements. Measurements obtained in curves are clipped from the graph. In turns the temperature sensor is influenced by an boundary layer from the UAS fuselage and the flow temperature measurements are compromised. Hence, the three data lags in each profile.

3.4 Data treatment and derived parameters

For the normalised residual horizontal wind speed u_r/u_0, both parameters have to be retrieved from the UAS measurements. Therefore, for each flight leg two regions have to be defined: one for the undisturbed flow velocity and one that represents the decrease in wind speed due to wind energy conversion. To facilitate identifying these regions the measured data is smoothed

5 out by a moving average of 200 data points (2 s). The undisturbed horizontal wind speed is then derived from the measurement for each flight leg individually that is not influenced by the wake. The reduced wind velocity u_r is derived from the minimum in the wake that results from the wind energy conversion. This method is used, since especially in the near wake, nacelle effects influence and increase the residual wind speed along the wake centre line. Figure 6 shows two exemplary wake measurements of the horizontal wind u_{hor} at distances $x/D = 2$ and $x/D = 5$. The residual and free stream wind velocity are indicated by

10 red and blue lines.

Table 1. Overview over model parameters used in this study.

Parameter	Frandsen et al. (2006)	Bastankhah and Porté-Agel (2014)	MaST	log. fit
u_* (m s^{-1})			0.25	0.29
z_0 (m)	0.0001		0.0001	0.0001
C_T (−)	0.7	0.7	0.7	
k (−)	0.037	0.178 (measured), 0.035 (best fit)		

Some measurements did not allow for a useful data evaluation, e.g. the aforementioned too short flight paths, unfinished turning manoeuvres of the UAS, data lags due to flow angles out of specification for the five-hole probe. Hence, all flights can lag data points at various distances in the evaluation. Some flight legs had to be discarded.

The model by Bastankhah and Porté-Agel (2014) allows for a measured wake growth rate k. This parameter is derived from the measurements shown in Fig. 6 and calculated to:

$$k = \frac{\Delta\text{wake}}{\Delta x} \approx \frac{61 \text{ m}}{342 \text{ m}} = 0.178 \tag{29}$$

The thrust coefficient C_T of the E-112 WEC is derived from the operational conditions at the time of the measurement flights. Therefore the tip-speed ratio (TSR) λ is calculated using a rotational velocity of 12 revolutions per minute (rpm), the rotor radius R and an average wind velocity of 11 m s^{-1}.

$$\lambda = \frac{\Omega R}{u_0} = 2\pi \frac{12 \cdot 57 \text{ m}}{60 \text{ s} \cdot 11 \text{ m s}^{-1}} \approx 6.5 \tag{30}$$

The TSR is now used to estimate the thrust coefficient using an C_T-TSR chart of the very similar NREL 5 MW WEC (Al-Solihat and Nahon, 2018) and a pitch angle $\beta = 1°$ yielding a thrust coefficient $C_T \approx 0.7$. The same method has been applied previously in Mauz et al. (2019). All parameters that are used in this study are shown in Tab. 1. Note that the friction velocity used in the MaST calculations has been lowered to fit the data better, to counteract the dyke effect and to represent a typical value found in neutral atmospheric conditions.

4 Results

In this section the MASC measurements are compared to two conventional wake models and two analytical solutions (one with constant and one with dynamic α as seen in Eq. 23) and the numerical solutions (Eq. A3 and Eq. A7) of the simplified momentum flux conservation equation. It can be shown that Euler forward and backward method are identical. Both introduce a small error that increases with increasing Δx. However, the analytical solution Eq. 21 is not far off from the numerical solution. In the presented data the maximum deviation between the analytical and numerical solution is $\Delta_{\max} \approx 5\,\%$ at 5 D. An
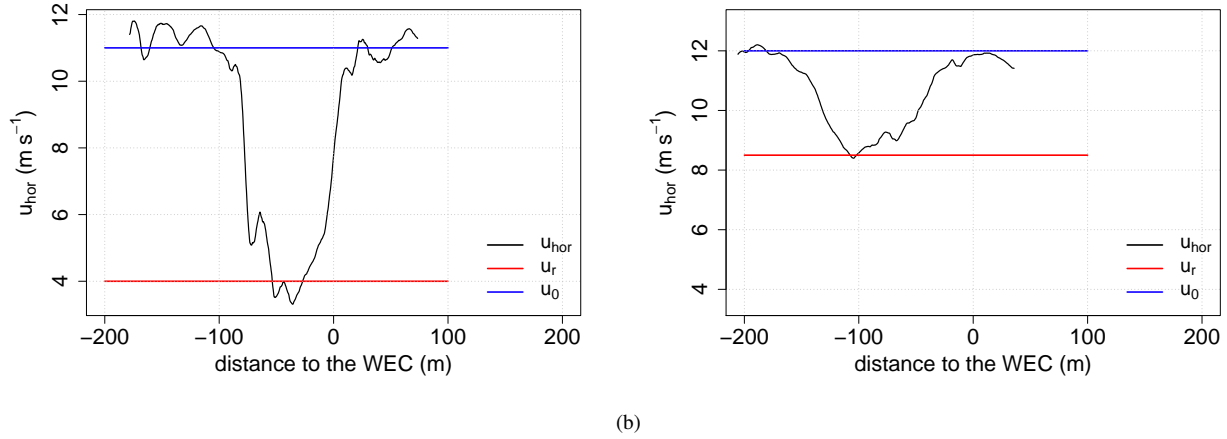
Figure 6. UAS measurements with a 2 s moving average to retract turbulence of the horizontal wind velocity u_{hor} at $x/\mathrm{D} = 2$ **(a)** and $x/\mathrm{D} = 5$ **(b)**.

additionally occurring parameter in the equations is the hub height of the E-112 converter. This hub height is set to $h = 125$ m. In the $\alpha = \mathrm{const.}$ calculations, $d(x)$ is set to half a rotor diameter throughout the calculations.

The analytical solutions are based on Eq. 21 which is a simplified solution of the differential equation 19. However, the constant C, appearing in Eq. 19 and in Eq. 23 needs adjustment when applying the model to real-world conditions. The constant $C = 8$

5   as derived above is only true, when considering that the momentum influx from all directions is equally pronounced (we recall the rotational symmetry of the wake in the derivation of the model). Yet, in a real-world scenario the momentum influx from below is limited by the vicinity of the ground and usually lower wind velocities, in contrast to the constant downward influx from aloft from the free stream. A similar argument can be made for the lateral momentum influx that is not as quickly replenished from the sides as the vertical momentum influx that is constantly filling up the wake. Due to these reasons a value

10   of $C < 8$ is more realistic. Following these arguments C has been halved due to the almost non-existent momentum influx from below and halved again due to the almost non-existent lateral replenishment of momentum flux outside of the wake, yielding $C = 2$ which is used in all calculations.

4.1 The conventional wake models

In Fig. 7 the Frandsen et al. (2006) and the Bastankhah and Porté-Agel (2014) model (with measured k) do not represent the

15   measured data very well. Both models overestimate the wind deficit decay in the near wake but might represent the far wake from $5 - 6$ D onwards adequately. However, there is no data to support this region sufficiently.

The model by Bastankhah and Porté-Agel (2014) can be fitted by lowering the wake growth rate k and discarding the measured value. Then the model describes the wake from 3 D onwards quite well, which is also the minimum distance that Bastankhah and Porté-Agel (2014, 2017) claim for their model.

4.2 MaST solutions using a constant α

The assumption of a constant α is the simplest approach, but neglects the measurements of Lignarolo et al. (2014); Medici and Alfredsson (2006) and the theory by Frandsen (2007) who studied i.a. turbulence entrainment in the near wake. The grey solid line in Fig. 7 shows the analytical model for the constant-α solution. The Euler series for this solution is not shown to avoid

5 cluttering the graph. The analytical solution fits the data well up to the point where free-stream turbulence has an influence on to wind deficit. From the measured data, this distance can be derived to be about $2 - 3$ D $\approx 230 - 300$ m. From this point on, both calculated solutions seem to no longer represent the measured data. This is also the region in which the helical tip vortex structure has collapsed, lost its rotational momentum and can no longer shield the wind deficit from the surrounding flow turbulence and shear. This region also depends on the tip speed ratio and therefore is variable and coupled to the wind

10 conditions and the operation of the WEC (Porté-Agel et al., 2020).

4.3 MaST solutions using a dynamic α

To represent the MASC data and to do justice to the entraining turbulence, accelerating the wind deficit decay, Eq. 21 and Eq. 20.1 need a slight modification. Now, Eq. 25 is used, thus, α defined in Eq. 23, is now a function of x. As described above, d corresponds to the radius in the wake of 'pure wake turbulence', still knowing its origin. With this parameter decreasing

15 downwind of the wake, α increases along the x axis. This essentially creates a high turbulent region in which the turbulent momentum flux from aloft and the sides increases the decay of the wind deficit and conversely increases the mean horizontal wind. The black solid line in Fig. 7 shows the result of an increasing α in the MaST solution, using $d(x)$ as defined by Eq. 25 and shown in Fig. 2. The analytical and the numerical solution now follow the measured data. The measured data scatter about ± 5 % around the computed solutions. The most important feature is the kink at $x = 2$ D, where both solutions are adjusted

20 by considering the entraining free-stream turbulence, following the progressively decreasing wind deficit by an increase of the residual wind speed in the wake.

4.4 Far wake behaviour of the MaST model

In the sections above, the behaviour of the models is described up to 5 D from the WEC. For the far wake there are no data available, due to legal limitations and flight regulations at the measurement site. In general, the far wake of a single WEC,

25 roughly beginning at $8 - 10$ D and beyond, is characterised by 'uniform' turbulence, meaning that atmospheric turbulence and turbulence created by the WEC are theoretically undistinguishable from one-another. The additionally created turbulence by the WEC has almost dissipated and the wake stream is reintegrated into the surrounding flow. Figure 7 shows the behaviour of all models including the MaST solutions for constant and dynamic α up to the far wake. While the constant-α MaST model underestimates the wake behaviour, the dynamic-α approach follows the measured data up to ≈ 5 D. Eventually, the numerical

30 solution runs into saturation at $u_r/u_0 = 0.95$ at about 10 D.

WIND
ENERGY
SCIENCE
DISCUSSIONS
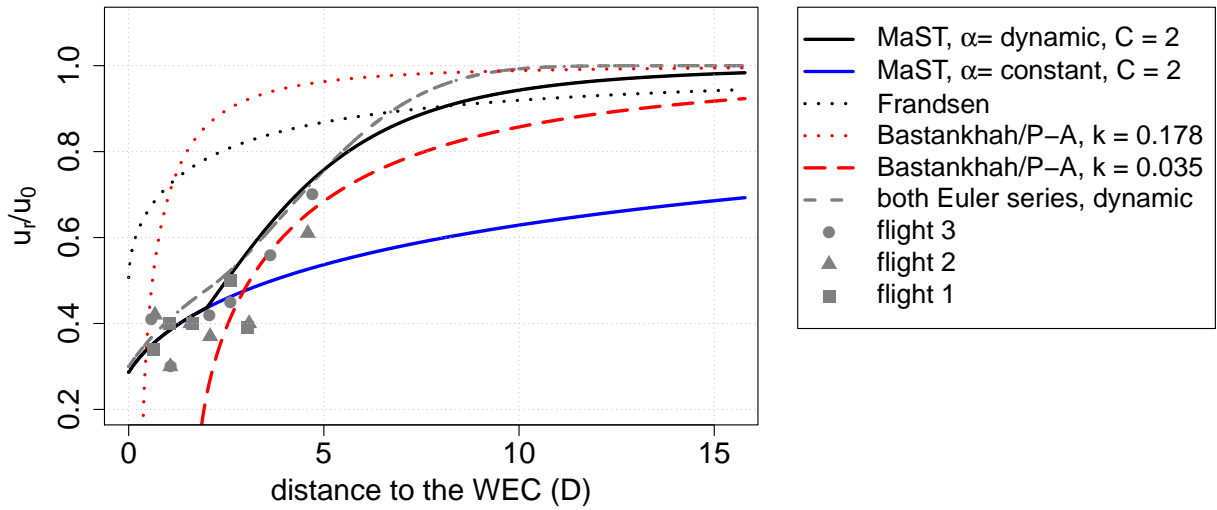
Figure 7. Normalised reduced wind speed measurements of three flights at hub height behind an Enercon E-112 WEC (grey points). The analytical and numerical model use a dynamic α (black solid line) to satisfy for a decreasing turbulence thickness d for increasing x. In direct comparison to the constant-α solution (solid grey line) the dynamic-α solution follows the measured data.The implementation of a dynamic α satisfies for the change in turbulence entrainment from around 2.5 D. The free stream velocity of $0.95 \cdot u_0$ in the wake is reached at ca. 10 D in the analytical solution. Also the numerical model reaches its saturation of $u_r/u_0 = 0.95$ at around 8 D. Conventional wake models are additionally shown.

5   Discussion

The presented analytical and numerical solution for the MaST model shown in Sec. 4 acknowledge the near-wake turbulence behaviour. As shown above, the adjusted model (which uses a changing α along the wake) follows the measured in-situ data. The far wake behaviour of the dynamic-α model paints a reasonable picture of the wind deficit decay, indicating a wake length

5   of roughly 10 D which is a common wake length in neutral conditions (McKay et al., 2012). This solution facilitates, in a first approach, a rather simple hyperbolic function (Eq. 25) to simulate the decrease of WEC turbulence along x. A linear function (or decrease) has been discarded, because this would require a distinct intersection point at some distance x/D. Consequently, a distance would have had to been defined where $\Delta z = 0$. Such an approach would have contradicted the idea of a dynamic α. As of now, the resulting function that is used to describe the remaining untouched WEC turbulence (with unit length) is not

10   continuously differentiable. However, in this semi-numerical implementation this is not necessary. Also there most certainly exists a smoother function that simulates the same behaviour which could be a task for a future evaluation.

The presented model can further be understood as a simple solution of the momentum conservation equation for a specific initial condition. The resulting equations are the solution of the simplified momentum conservation equation for the atmospheric flow that has been brought out of its equilibrium. The presented solutions also represent the shear stress that is created by the WEC itself (solely by its presence in the flow). We recall the C parameter in Eq. 19.

5   The likely solution of the simplified Navier-Stokes equation simulates the surrounding atmosphere refilling a 'velocity gap', created by a horizontal wind depression in flow direction ($u_r(0) = 0.3\ u_0$). In the mathematical derivation of the model a rotational symmetric wake has been assumed, which is realistic. But also a rotational symmetric momentum influx has been assumed, which is helping the mathematical derivation, but is not too realistic, and leads to $C = 8$ in Eq. 19. To prevent an over-pronunciation of momentum influx $C = 2$ has been used throughout this study. The results show that even a value of

10    $1 < C < 2$ could provide a better fit.

    To implement a shear or friction velocity Eq. 26 has been used. This equation is only valid in the surface layer (or Prandtl layer) and could be applied up to the inversion height z_i. The assumption was made that the WEC was still in the surface layer in order to derive the model. The authors are aware that the validity of the equation is stretched in this work. As a consequence K_m might be over estimated (by using a too large, out of scope value for z), thus, Δz is under estimated (e.q. in Eq. 23). The

15   application of Eq. 26 could be circumvent by using a proper ground measurement of u_*, e.g. by using an EC (eddy-covariance) station. The friction velocity was only available from a vertical profile, flown by the UAS in front of the WEC. The influence of the shear velocity u_* has been examined by changing the input value by $\pm 50\%$. The resulting analytical solutions then change their slope which then results in different wake lengths. The calculated wake lengths differ around $\pm 3 - 4$ D. Longer wakes are calculated for stable atmospheric conditions and smaller wake lengths for unstable conditions. For the sensitivity calculation

20   the distance where atmospheric turbulence could act on the wake deficit was kept at 2 D. In reality this distance would be a function of the tip-speed ratio λ (tip-speed of blade normalised by the horizontal wind speed) and the atmospheric thermal stability.

    The second parameter influencing the wind deficit decay rate α is the separation height Δz or in this study later called the turbulence thickness height d. In Emeis (2010, 2017) Δz is the distance from hub height to the layer above the wind park wake

25   which introduces vertical turbulent momentum flux into the wake, resulting in a wind deficit decay. In this study, only a single turbine is considered. Instead of speculating about the dimensions of the separation height, an unquestionable boundary, the boundary between the wake centre line (deficit) and the undisturbed flow, is chosen to be represented by d. The distance d has an additional meaning in this study: it represents the radius of the WEC turbulence, measured from the wake centre. In the above paragraph K_m and u_* are discussed. Together with d those parameters control the wind deficit decay rate $\alpha = C \cdot K_m/d^2$.

30   For fitting purposes α can be treated as a black box, thus, it does not matter, if K_m is overestimated and d underestimated. Consequently, the model could be fed with measured values at hub height (e.g. for K_m) to study the separation height Δz in the future. But in the present study, empirical relations and most probable values for parameters derived from secondary results (virtual potential temperature profile) were used to quantify α.

    The wind vector calculation relies on a constant relative true air speed (TAS) of the UAS of $18.5 \ \mathrm{m\,s^{-1}}$. When leaving

35   and entering a wake, the TAS does change quickly. The error in wind velocity calculation is around 10% (Rautenberg et al.,

2019a). Since in this study the residual wind speed in the wake is a normalised parameter and the undisturbed free stream velocity suffers the same error, the error can be assumed as insignificant.

The conventional WEC wake models, as shown also in this study, primarily use operational parameters like the thrust coefficient, pitch angle, and wake growth rate etc. to determine the momentum conversion of the WEC and the resulting initial
5 wind deficit. From thereon, usually an empirical exponential decay or square-root function is used to describe the wind deficit. The atmosphere and its properties are not considered in these models. The analytical solution proposed in this study tries to provide a more profound model based on the conservation of momentum in the atmosphere. Eventually, both model approaches could be combined in the future.

6 Conclusions

10 The derived analytical solution shows good agreement with the in-situ UAS measurements and plausible behaviour in the far wake. It is shown that in the wake, that the free-stream turbulence is unable to affect the wind deficit in the near wake. In the mid wake atmospheric turbulence and momentum affect the development of the wind deficit. Although the lack of data for the far wake, the dynamic-α model connects the near wake with the intermediate and far wake turbulence and wind deficit. In future UAS measurements the wake development farther down the wake would be interesting to cover as well, e.g. up to
15 $10 - 15$ D.

Regarding the far wake behaviour of the dynamic-α approach, it could be shown, that the analytical and numerical solution can predict a capped internal boundary layer. One of the main features of this approach (e.g. for an internal boundary layer model) is the capability to reach a certain saturation level. This can be a great advantage in modelling wind transitions from land to sea (or vice versa) or thermal internal boundary layers (TIBL) in general.

20 The model presented in this case can also be applied to larger scale problems. For example to describe the wind deficit of a wind farm by altering Eq. 12, which is investigated in an additional study.

In the future the presented model could be combined with conventional existing momentum sink models to get a description of operating WEC and its surrounding flow.

Data availability. The measured UAS data can be provided by the authors (Moritz Mauz, Jens Bange, Andreas Platis) by ftp. Due to the
25 amount and complexity of the data, we advise a brief introduction by one of the authors.

Appendix A: Euler method

The Euler method is a simple way to solve differential equations of first order numerically (Atkinson et al., 2009; Faragó, 2013). Thus, this method can solve the presented Eq. 20.1 numerically. :

$$u(x)' = f(u(x)) \tag{A1}$$

The dash denotes a continuously differentiable derivation of $u(x)$. Discretising each calculation step with:

$$x_n = x_0 + h\,n, \text{ with } n = 1, 2, 3, ...$$ (A2)

The differential form is approximated by a discrete expression, with a discretisation step $h = 0.1$ m in the presented study.

$$\frac{u(x_{n+1}) - u(x_n)}{h} \approx f(u(x_n)) \;\Rightarrow\; u(x_{n+1}) \approx u(x_n) + h\,f(u(x_n))$$ (A3)

5 Reducing h further does not change the result, but increases the computation time. Thus, the step size $h = 0.1$ m is used for the numerical solutions. Both, the forward and backward method, are used to validate the analytical solution and to obtain a numerical solution for the difference Eq. 20.1, a short derivation of the specific Euler solutions is shown below.

Inserting Eq. 20.1 in Eq. A3 with $\Delta x = h$ and $u = u_r$ the Euler forward solution is:

$$u(x_{n+1}) \approx u(x_n) + h\left(\frac{\alpha u_0}{2u(x_n)} - \frac{\alpha}{2}\right)$$ (A4)

10 While Eq. A3 is called the Euler forward or explicit method, also an Euler backward or implicit method (Eq. A5) is calculated, where the solution is only available implicitly, hence the name. While the Euler forward method is straight forward and simple to solve, for the Euler backward solution Eq. A5 has to be solved for $u(x_{n+1})$. Note the appearance of $u(x_{n+1})$ on both sides of the equation.

$$u(x_{n+1}) \approx u(x_n) + h\,f(u(x_{n+1}))$$ (A5)

15 Re-writing Eq. A4 for the backward solution method yields:

$$u(x_{n+1}) \approx u(x_n) + h\left(\frac{\alpha\,u_0}{2\,u(x_{n+1})} - \frac{\alpha}{2}\right)$$ (A6.1)

$$\approx u(x_n) + \frac{h\alpha\,u_0}{2u(x_{n+1})} - \frac{h\alpha}{2}$$ (A6.2)

Multiplying both sides of the equation with $u(x_{n+1})$

$$\Longleftrightarrow u(x_{n+1})^2 \approx u(x_{n+1}) \cdot u(x_n) + \frac{h\alpha\,u_0}{2} - \frac{h\alpha\,u(x_{n+1})}{2}$$ (A6.3)

20 Rearranging to a quadratic equation gives:

$$\Longleftrightarrow u(x_{n+1})^2 - u(x_{n+1})\left(u(x_n) - \frac{h\alpha}{2}\right) - \frac{h\alpha\,u_0}{2} \approx 0$$ (A6.4)

The resulting specific Euler backward solution is the positive version of the solution of the quadratic Eq. A6.4:

$$u(x_{n+1}) = \frac{u(x_n) - \frac{h\alpha}{2} \pm \sqrt{\left(u(x_n) - \frac{h\alpha}{2}\right)^2 + 2\alpha u_0 h}}{2}$$ (A7)

Author contributions. MM evaluated the UAS data and derived the formalism. BvK supported the methods with his expertise and his ABL
25 knowledge. AP added to the discussion and understanding of the topic. SE and JB shaped the manuscript and added valuable input to form an enclosing theme. All authors added constructive criticism during the process of writing the manuscript.

Competing interests. The authors declare that they do not have competing interests.

Acknowledgements. Financial support: This research has been supported by the Projektträger Jülich, the BMWi (Federal Ministry for Economic Affairs and Energy) that funded the HeliOW project (0324121C).

This open-access publication was funded by the University of Tübingen.

References

Al-Solihat, M. K. and Nahon, M.: Flexible Multibody Dynamic Modeling of a Floating Wind Turbine, International Journal of Mechanical Sciences, 142–143, 518–529, https://doi.org/10.1016/j.ijmecsci.2018.05.018, 2018.

Atkinson, K., Han, W., and Stewart, D.: Numerical solution of ordinary differential equations, John Wiley and Sons, Inc., Hoboken, New Jersey, USA, https://doi.org/10.1007/978-3-540-75979-9, 2009.

Bärfuss, K., Hankers, R., Bitter, M., Feuerle, T., Schulz, H., Rausch, T., Platis, A., Bange, J., and Lampert, A.: In-situ airborne measurements of atmospheric and sea surface parameters related to offshore wind parks in the German Bight, https://doi.org/10.1594/PANGAEA.902845, https://doi.org/10.1594/PANGAEA.902845, 2019.

Bastankhah, M. and Porté-Agel, F.: A new analytical model for wind-turbine wakes, Renewable Energy, 70, 116 – 123, https://doi.org/https://doi.org/10.1016/j.renene.2014.01.002, special issue on aerodynamics of offshore wind energy systems and wakes, 2014.

Bastankhah, M. and Porté-Agel, F.: A New Miniature Wind Turbine for Wind Tunnel Experiments. Part II: Wake Structure and Flow Dynamics, Energies, 10, 923, https://doi.org/10.3390/en10070923, 2017.

Betz, A.: Das Maximum der theoretisch möglichen Ausnützung des Windes durch Windmotoren, Zeitschrift für das gesamte Turbinenwesen, 26, 307–309, 1920.

Betz, A.: The Maximum of the Theoretically Possible Exploitation of Wind by Means of a Wind Motor, Wind Engineering, 37, 441–446, https://doi.org/10.1260/0309-524X.37.4.441, 2013.

Braam, M., Beyrich, F., Bange, J., Platis, A., Martin, S., Maronga, B., and Moene, A. F.: On the Discrepancy in Simultaneous Observations of the Structure Parameter of Temperature Using Scintillometers and Unmanned Aircraft, Boundary-Layer Meteorology, 158, 257–283, https://doi.org/10.1007/s10546-015-0086-9, 2016.

Brand, A. J., Peinke, J., and Mann, J.: Turbulence and wind turbines, Journal of Physics: Conference Series, 318, 072 005, https://doi.org/10.1088/1742-6596/318/7/072005, https://doi.org/10.1088%2F1742-6596%2F318%2F7%2F072005, 2011.

Canadillas, B., Foreman, R., Barth, V., Siedersleben, S., Lampert, A., Platis, A., Djath, B., Schulz-Stellenfleth, J., Bange, J., Emeis, S., and Neumann, T.: Offshore wind farm wake recovery: Airborne measurements and its representation in engineering models, Wind Energy, 23, https://doi.org/10.1002/we.2484, 2020.

Cormier, M., Caboni, M., Lutz, T., Boorsma, K., and Krämer, E.: Numerical analysis of unsteady aerodynamics of floating offshore wind turbines, Journal of Physics: Conference Series, 1037, 072 048, http://stacks.iop.org/1742-6596/1037/i=7/a=072048, 2018.

Emeis, S.: A simple analytical wind park model considering atmospheric stability, Wind Energy, 13, 459–469, https://doi.org/10.1002/we.367, https://onlinelibrary.wiley.com/doi/abs/10.1002/we.367, 2010.

Emeis, S.: Wind Energy Meteorology, Springer, Heidelberg, Germany, 2017.

Faragó, I.: Note on the Convergence of the Implicit Euler Method, Numerical Analysis and Its Applications. NAA 2012. Lecture Notes in Computer Science, 8236, https://doi.org/https://doi.org/10.1007/978-3-642-41515-9_1, 2013.

Foken, T.: Angewandte Meteorologie, Springer-Verlag Berlin Heidelberg, https://doi.org/10.1007/978-3-642-25525-0, 2006.

Frandsen, S., Barthelmie, R., Pryor, S., Rathmann, O., Larsen, S., Højstrup, J., and Thøgersen, M.: Analytical modelling of wind speed deficit in large offshore wind farms, Wind Energy, 9, 39–53, https://doi.org/10.1002/we.189, 2006.

Frandsen, S. T.: Turbulence and turbulence-generated structural loading in wind turbine clusters, Risoe National Lab., Roskilde, Denmark. Wind Energy Dept.; Danmarks Tekniske Univ., Kgs. Lyngby, 2007.

Garratt, J.: Review: the atmospheric boundary layer, Earth-Science Reviews, 37, 89 – 134, https://doi.org/https://doi.org/10.1016/0012-8252(94)90026-4, http://www.sciencedirect.com/science/article/pii/0012825294900264, 1994.

Garratt, J. R.: The stably stratified internal boundary layer for steady and diurnally varying offshore flow, Boundary-Layer Meteorology, 38,
5   369–394, https://doi.org/https://doi.org/10.1007/BF00120853, 1987.

Hanna, S. R.: An empirical formula for the height of the coastal internal boundary layer, Boundary-Layer Meteorology, 40, 205–207, https://doi.org/https://doi.org/10.1007/BF00140077, 1987.

Horvat, B., Hajek, M., and Rauleder, J.: Analysing Rotorcraft Vortex Encounter Methods with a Lattice-Boltzmann Method Based GPU Framework, https://doi.org/10.2514/6.2020-0539, https://arc.aiaa.org/doi/abs/10.2514/6.2020-0539, 2020.

10   Jensen, N.: A note on wind generator interaction, no. 2411 in Risø-M, Risø National Laboratory, 1983.

Johnson, P. B., Jonsson, C., Achilleos, S., and Eames, I.: On the spread and decay of wind turbine wakes in ambient turbulence, Journal of Physics: Conference Series, 555, 012 055, https://doi.org/10.1088/1742-6596/555/1/012055, https://doi.org/10.1088/1742-6596/555/1/012055, 2014.

Lecheler, S.: Numerische Strömungsberechnung, Springer Vieweg, Wiesbaden, Germany, https://doi.org/10.1007/978-3-658-05201-0, 2011.

15   Lignarolo, L., Ragni, D., Krishnaswami, C., Chen, Q., Simão Ferreira, C., and van Bussel, G.: Experimental analysis of the wake of a horizontal-axis wind-turbine model, Renewable Energy, 70, 31 – 46, https://doi.org/https://doi.org/10.1016/j.renene.2014.01.020, http://www.sciencedirect.com/science/article/pii/S0960148114000494, special issue on aerodynamics of offshore wind energy systems and wakes, 2014.

Magnusson, M. and Smedman, A.-S.: Air flow behind wind turbines, Journal of Wind Engineering and Industrial Aerodynamics, 80, 169 –
20   189, https://doi.org/https://doi.org/10.1016/S0167-6105(98)00126-3, 1999.

Mauz, M., Rautenberg, A., Platis, A., Cormier, M., and Bange, J.: First identification and quantification of detached-tip vortices behind a wind energy converter using fixed-wing unmanned aircraft system, Wind Energy Science, 4, 451–463, https://doi.org/10.5194/wes-4-451-2019, https://www.wind-energ-sci.net/4/451/2019/, 2019.

McKay, P., Carriveau, R., Ting, D. S.-T., and Newson, T.: Turbine Wake Dynamics, IntechOpen, 10 Lower Thames Street, London, EC3R
25   6AF, UK, https://doi.org/10.5772/53968, 2012.

Medici, D. and Alfredsson, P. H.: Measurements on a wind turbine wake: 3D effects and bluff body vortex shedding, Wind Energy, 9, 219–236, https://doi.org/10.1002/we.156, https://onlinelibrary.wiley.com/doi/abs/10.1002/we.156, 2006.

Pixhawk-Organisation: PixHawk 2.1 Autopilot description, http://pixhawk.org, accessed: 2019-07-01, 2019.

Platis, A., Siedersleben, S. K., Bange, J., Lampert, A., Bärfuss, K., Hankers, R., Canadillas, B., Foreman, R., Schulz-Stellenfleth, J., Djath,
30   B., Neumann, T., and Emeis, S.: First in situ evidence of wakes in the far field behind offshore wind farms, Scientific Reports, 8, 2163, https://doi.org/10.1038/s41598-018-20389-y, 2018.

Porté-Agel, F., Bastankhah, M., and Shamsoddin, S.: Wind-Turbine and Wind-Farm Flows: A Review, Boundary-Layer Meteorology, 174, 1–59, https://doi.org/https://doi.org/10.1007/s10546-019-00473-0, 2020.

Rautenberg, A., Schön, M., zum Berge, K., Mauz, M., Manz, P., Platis, A., van Kesteren, B., Suomi, I., Kral, S. T., and Bange, J.: The
35   Multi-Purpose Airborne Sensor Carrier MASC-3 for Wind and Turbulence Measurements in the Atmospheric Boundary Layer, Sensors, 19, https://doi.org/10.3390/s19102292, http://www.mdpi.com/1424-8220/19/10/2292, 2019.

Rautenberg, A., Allgeier, J., Jung, S., and Bange, J.: Calibration Procedure and Accuracy of Wind and Turbulence Measurements with Five-Hole Probes on Fixed-Wing Unmanned Aircraft in the Atmospheric Boundary Layer and Wind Turbine Wakes, Atmosphere, 10, https://doi.org/10.3390/atmos10030124, http://www.mdpi.com/2073-4433/10/3/124, 2019a.

Siedersleben, S. K., Platis, A., Lundquist, J. K., Lampert, A., Bärfuss, K., Cañadillas, B., Djath, B., Schulz-Stellenfleth, J., Bange, J., Neumann, T., and Emeis, S.: Evaluation of a Wind Farm Parametrization for Mesoscale Atmospheric Flow Models with Aircraft Measurements, Meteorologische Zeitschrift, 27, 401–415, https://doi.org/10.1127/metz/2018/0900, 2018.

5 Stevens, R. J. A. M.: Dependence of optimal wind turbine spacing on wind farm length, Wind Energy, 19, 651–663, https://doi.org/10.1002/we.1857, 2016.

Strbac, A., Martini, T., Greiwe, D., Hoffmann, F., and Jones, M.: Analysis of Rotorcraft Wind Turbine Wake Encounters using Piloted Simulation, in: 45th European Rotorcraft Forum, https://elib.dlr.de/131134/, 2019.

Stull, R. B.: An introduction to boundary layer meteorology, Kluwer Academic Publishers, Dordrecht, the Netherlands,
10 https://doi.org/https://doi.org/10.1007/978-94-009-3027-8, 1988.

Wang, C., Campagnolo, F., Canet, H., Barreiro, D. J., and Bottasso, C. L.: How realistic are the wakes of scaled wind turbine models?, Wind Energy Science Discussions, 2020, 1–27, https://doi.org/10.5194/wes-2020-115, https://wes.copernicus.org/preprints/wes-2020-115/, 2020.

Wildmann, N., Mauz, M., and Bange, J.: Two fast temperature sensors for probing of the atmospheric boundary layer using small re-
15 motely piloted aircraft (RPA), Atmospheric Measurement Techniques, 6, 2101–2113, https://doi.org/10.5194/amt-6-2101-2013, https://www.atmos-meas-tech.net/6/2101/2013/, 2013.

Wildmann, N., Hofsäß, M., Weimer, F., Joos, A., and Bange, J.: MASC; a small Remotely Piloted Aircraft (RPA) for wind energy research, Advances in Science and Research, 11, 55–61, https://doi.org/10.5194/asr-11-55-2014, http://www.adv-sci-res.net/11/55/2014/, 2014a.

Wildmann, N., Ravi, S., and Bange, J.: Towards higher accuracy and better frequency response with standard multi-hole probes in turbulence
20 measurement with remotely piloted aircraft (RPA), Atmospheric Measurement Techniques, 7, 1027–1041, https://doi.org/10.5194/amt-7-1027-2014, http://www.atmos-meas-tech.net/7/1027/2014/, 2014b.

Wildmann, N., Rau, G. A., and Bange, J.: Observations of the Early Morning Boundary-Layer Transition with Small Remotely-Piloted Aircraft, Boundary-Layer Meteorology, 157, 345–373, 2015.

Wu, J.-S. and Faeth, G. M.: Sphere wakes at moderate Reynolds numbers in a turbulent environment, AIAA Journal, 32, 535–541, https://doi.org/10.2514/3.12018, https://doi.org/10.2514/3.12018, 1994.